PNAS RESEARCH ARTICLE | BIOPHYSICS AND COMPUTATIONAL BIOLOGY

Depletion-induced interactions modulate nanoscale protein diffusion in polymeric crowder solutions

Michelle Dargasz[a,1], Nimmi Das Anthuparambil[a,b], Sebastian Retzbach[c], Anita Girelli[d], Sonja Timmermann[a], Johannes Möller[e], Wonhyuk Jo[e], Aliaksandr Leonau[a,e], Mohammad Raza Agha[a], Maddalena Bin[d], Jaqueline Savelkouls[f], Iason Andronis[d], Frederik Unger[a,b], Felix Brausse[e], Jörg Hallmann[e], Ulrike Boesenberg[e], Jan-Etienne Pudell[e], Angel Rodriguez-Fernandez[e], James Wrigley[e], Roman Shayduk[e], Mohamed Youssef[e], Alexey Zozulya[e], Anders Madsen[e], Felix Lehmkühler[b], Fivos Perakis[d], Fajun Zhang[c], Frank Schreiber[c], Michael Paulus[f], and Christian Gutt[a,1]

Affiliations are included on p. 10.

Edited by Steve Granick, University of Massachusetts at Amherst, Amherst, MA; received September 9, 2025; accepted June 29, 2026

Macromolecular crowding plays a crucial role in modulating protein dynamics in cellular and in vitro environments. Polymeric crowders such as dextran and Ficoll are known to induce entropic forces, including depletion interactions, that promote structural organization, yet their nanoscale consequences for protein dynamics remain poorly understood. Here, we employ megahertz X-ray photon correlation spectroscopy (MHz-XPCS) at the European X-ray Free Electron Laser (XFEL) to probe the dynamics of the protein ferritin in solutions containing sucrose, dextran, and Ficoll. We find pronounced changes in collective protein dynamics in polymeric crowders, revealing depletion-driven short-range attractions that, combined with long-range repulsions, give rise to intermediate-range organization. These mesoscale correlations undergo collective relaxation on microsecond to millisecond timescales, as directly resolved by XPCS through the decay of ferritin density fluctuations. The magnitude of this depends sensitively on crowder molecular weight and type. Normalizing the crowder concentration by c^* reveals scaling behavior of ferritin self-diffusion with a crossover near $2c^*$, marking a transition from depletion-enhanced mobility to viscosity-dominated slowing. Our results demonstrate that bulk properties alone are insufficient to describe protein dynamics in crowded solutions, highlighting the need to include polymer-specific interactions and depletion theory in models of crowded environments.

macromolecular crowding | diffusion | depletion interaction | X-ray photon correlation spectroscopy | free electron laser

Significance

Understanding how proteins move and interact in crowded environments is essential for unraveling the physical basis of cellular processes. Polymeric crowders are widely used to mimic intracellular crowding, yet their effects are often interpreted primarily in terms of static structure or macroscopic viscosity. Using megahertz X-ray photon correlation spectroscopy, we show that protein dynamics are modulated by depletion interactions that give rise to transient mesoscale organization, as revealed through their impact on collective and self-diffusion. Polymer molecular weight and type emerge as key control parameters governing these effects. Our results provide a framework for incorporating polymer physics and depletion theory into models of crowded environments, enabling improved connections between in vitro experiments and the dynamic complexity of the cellular interior.

Macromolecular crowding is a defining feature of cellular environments (1–6), where high concentrations of macromolecules strongly influence protein dynamics (7–12)—a key factor in processes such as molecular transport, signal transduction, and enzymatic activity (13–15). Numerous studies have demonstrated that crowding can, for instance, modulate biochemical reactions by hindering protein diffusion or enhancing complex formation through a combination of excluded-volume effects, entropic and enthalpic interactions (16–19). To mimic such crowded conditions in vitro, polymeric crowders such as polyethylene glycol (PEG), Ficoll, and dextran are widely employed (20–22), and their impact on protein structure and thermodynamics has been extensively characterized.

In protein-polymer mixtures, nonadsorbing polymers induce depletion interactions that generate short-range attractions between proteins (23–29). These interactions are known to promote protein–protein association, clustering, and liquid–liquid phase separation (LLPS) (30–34), whose structural consequences have been studied in detail using scattering techniques (35, 36). In particular, when short-range attractions are counterbalanced by long-range repulsions, proteins may develop intermediate-range order (IRO), which manifests itself as a weak low-q feature in the static structure factor (35, 37). While such structural features are well documented, it remains largely unclear whether these weak static signatures correspond to dynamically relevant mesoscale organization or merely reflect time-averaged correlations with limited influence on protein mobility. In particular, the impact of such mesoscale correlations on protein dynamics at nanometer length scales and microsecond timescales—relevant for transient complex formation and transport in crowded environments—remains poorly understood.

A major limitation in addressing this question has been the lack of experimental access to protein dynamics in the regime where depletion-driven mesoscale organization

The authors declare no competing interest.

This article is a PNAS Direct Submission.

Copyright © 2026 the Author(s). Published by PNAS. This article is distributed under Creative Commons Attribution-NonCommercial-NoDerivatives License 4.0 (CC BY-NC-ND).

[1]To whom correspondence may be addressed. Email: michelle.dargasz@uni-siegen.de or christian.gutt@uni-siegen.de.

This article contains supporting information online at https://www.pnas.org/lookup/suppl/doi:10.1073/pnas.2524733123/-/DCSupplemental.

Published July 29, 2026.

Downloaded from https://www.pnas.org by Michelle Dargasz on July 30, 2026 from IP address 217.83.180.133.

emerges. Conventional optical techniques typically probe either single-particle diffusion on longer timescales or average transport properties governed by bulk viscosity, while scattering experiments primarily provide static structural information (35, 38, 39). As a result, the dynamic consequences of depletion interactions and IRO have so far been inferred indirectly or predicted by simulations (40), but remain largely unexplored experimentally.

Here, we address this gap by directly probing protein dynamics in crowded polymer solutions using megahertz X-ray photon correlation spectroscopy (MHz-XPCS) at an X-ray free-electron laser. MHz-XPCS provides access to density fluctuations on nanometer length scales and microsecond-millisecond timescales, enabling simultaneous measurements of collective and self-diffusion in highly concentrated solutions (41–43). Importantly, MHz-XPCS probes protein motion governed by the local, molecular-scale viscosity experienced by proteins rather than macroscopic bulk viscosities. This unique capability allows us to directly resolve the dynamic consequences of depletion-induced interactions and mesoscale structural organization.

Using ferritin as a monodisperse globular model protein, we investigate solutions containing small molecular crowders and polymeric polysaccharides of varying molecular weight and concentration. All experiments are performed at physiologically relevant protein concentrations, chosen to minimize self-crowding while retaining sensitivity to crowder-mediated interactions. We show that polymeric crowders induce depletion-driven short-range attraction combined with long-range repulsion, giving rise to intermediate-range order that is predominantly dynamic in nature. This transient mesoscale organization strongly suppresses collective diffusion on length scales of several protein diameters. Furthermore, we find that ferritin self-diffusion exhibits a nonmonotonic dependence on crowder concentration, reflecting nanoscale effects associated with a shrinking depletion layer thickness in the semidilute regime, followed by a crossover to macroscopic viscosity control in the concentrated regime. These deviations from simple linear scaling–resembling those observed for nanoparticles in PEG solutions (39)–highlight the importance of nanoscale interactions that can be directly resolved by XPCS.

Taken together, our results demonstrate that crowders profoundly shape protein dynamics through emergent structural organization and modifications of the local interaction landscape. These findings call for a refined framework for protein dynamics in crowded environments, in which depletion interactions, polymer network structure, and transient nanoscale order are treated as central elements governing protein mobility and phase behavior.

Results

Modeling a Crowded Environment Utilizing Crowding Agents. In this study, we investigated the protein ferritin, dissolved in solutions containing various macromolecular crowders. Ferritin is a spherical protein complex composed of 24 subunits that assemble into a hollow shell capable of storing up to 4,500 Fe(III) atoms (44, 45), thus fulfilling its primary function as iron storage (46). Its hydrodynamic radius has been determined to be R_h = 6.85 nm (47). Due to its monodispersity and stability over a broad range of pH and temperature conditions, ferritin is also widely used in vaccine development (48) and drug delivery applications (49, 50). These attributes, combined with the strong X-ray scattering contrast provided by its iron-rich core, make ferritin an ideal globular model protein for X-ray scattering studies under crowded conditions.

All experiments were conducted at a constant ferritin concentration of 55 mg/ml, corresponding to a protein volume fraction of approximately 2.55%v/v. At this concentration, self-crowding effects remain negligible while protein–protein interactions influenced by the crowders are still measurable, allowing us to isolate the dynamic effects of crowder-induced interactions. This concentration is also physiologically relevant, as cytoplasmic protein concentrations have been estimated to be on the order of 75 mg/ml (51).

Several standard crowding agents spanning a broad range of molecular sizes and architectures were used, including sucrose, a small nonpolymeric crowder (M_w = 342.3 g/mol), and the polysaccharides Ficoll400 (M_w = 400 kg/mol) and dextran with three different molecular weights (M_w = 40, 100, 500 kg/mol; in the following referred to as dextran 40, dextran 100, and dextran 500). Ficoll is a highly branched, internally cross-linked polymer with a compact conformation, whereas the branched dextrans form more flexible, extended structures (20, 52). The corresponding radii of gyration (R_g) and their ratio to that of ferritin are listed in Table 1 as reported in refs. 53–55, referring to the molecular dimensions in dilute systems.

We focused on crowder concentrations of 10 to 35%w/w (~9.5 to 30%v/v), corresponding to cytoplasmic macromolecular volume fractions of 20 to 40%v/v (1, 56, 57). Changes in the slope of the macroscopic viscosity measured across the full concentration range were used to estimate the overlap concentration c^* and entanglement concentration c^{**} for dextran, as summarized in Table 1. c^* of Ficoll was taken from ref. 58. Accordingly, the investigated solutions predominantly fall within the semidilute to concentrated polymer regime. The solvent quality corresponds to θ-solvent conditions.

Accessing Nanoscale Protein Dynamics by Extracting Intensity Autocorrelation Functions Utilizing XPCS. We investigated the influence of standard crowders on protein dynamics via MHz-XPCS experiments at the Materials Imaging and Dynamics (MID) instrument of the European XFEL (59). This technique enables direct access to collective and self-diffusion on nanometer length scales and microsecond timescales, even in highly concentrated solutions (60–65). Moreover, XPCS allows determination of the hydrodynamic function, aiding in the study of long-range many-body interactions mediated by the solvent (66). These capabilities make MHz-XPCS a powerful tool for investigating molecular crowding effects. Its successful application to protein dynamics has been demonstrated by Reiser et al. (41), Girelli et al. (42), and Anthuparambil et al. (43).

Samples were loaded into quartz-glass capillaries and sealed with epoxy glue. The experimental setup for MHz-XPCS experiments at MID is shown in Fig. 1*A*. Results are reported from two experimental campaigns using photon energies of 9 and 10 keV and beam sizes of 14.5 and 14.2 μm, respectively.

Table 1. Crowder-specific parameters

Crowder	R_g (nm)	$R_{g,ferr}/R_{g,cr}$	c^* (%w/w)	c^{**} (%w/w)
Sucrose	0.4	11.11	–	–
Ficoll	11.07	0.53	17	–
Dextran 40	6.2	0.95	12.75	31.42
Dextran 100	9.5	0.62	9.42	26.09
Dextran 500	20	0.29	4.97	18.11

Downloaded from https://www.pnas.org by Michelle Dargasz on July 30, 2026 from IP address 217.83.180.133.

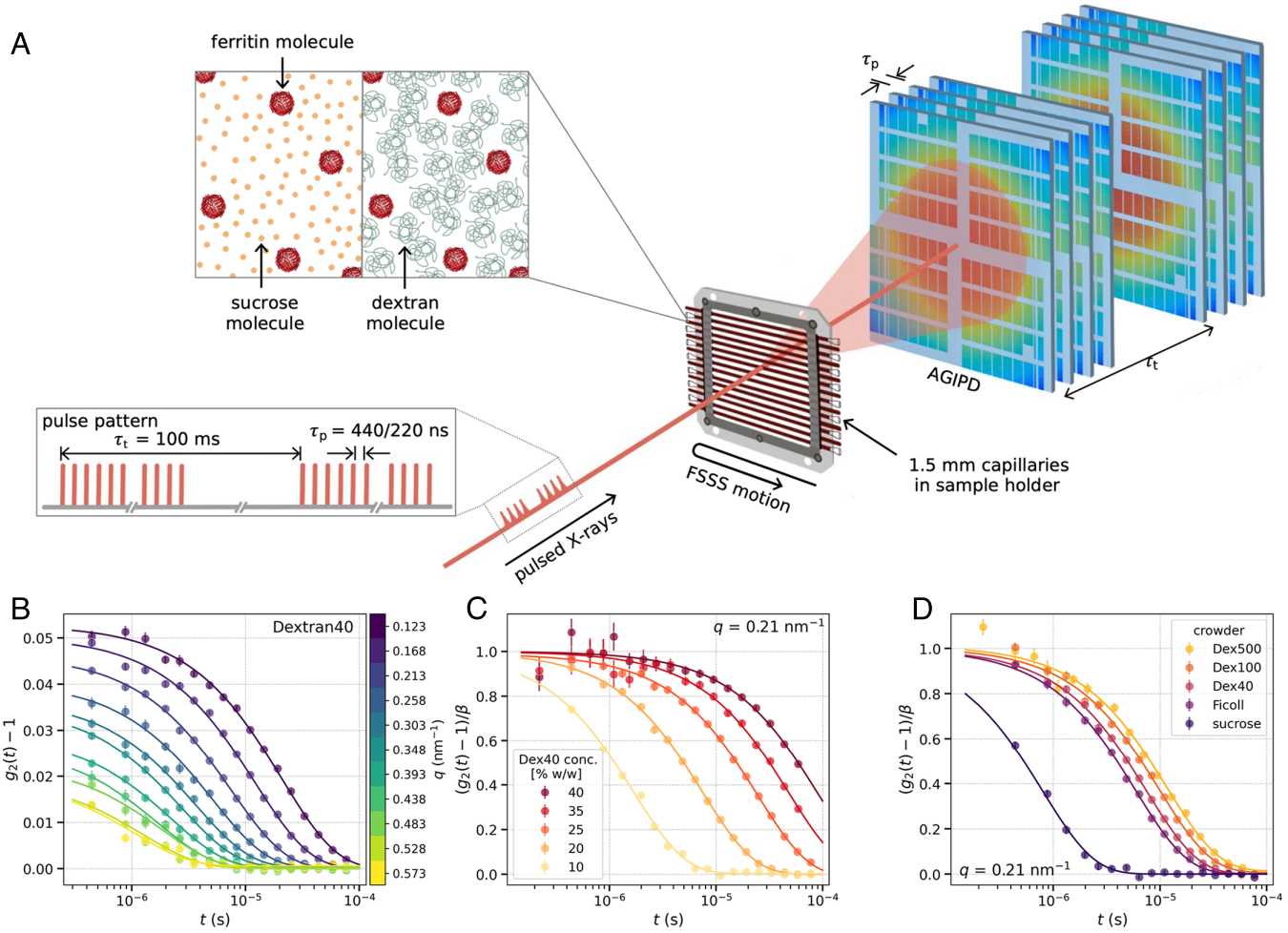


Fig. 1. MHz-XPCS measurements at the MID instrument of the European XFEL. (*A*) Schematic of the experimental setup. Coherent X-ray pulses illuminate ferritin solutions containing different crowder types and concentrations, producing speckle patterns recorded by the AGIPD. A new pulse train is delivered every 100 ms, with intrapulse spacings of 440 ns and 220 ns used. The Fast Solid Sample Scanner (FSSS) moves the sample between trains, ensuring that each train probes a fresh spot. Intensity fluctuations within a train are analyzed to extract dynamic information by calculating intensity autocorrelation functions ($g_2(t)$). (*B*) q-dependent $g_2(t)$ functions for ferritin in a 25%w/w dextran 40 solution. (*C*) $g_2(t)$ functions at a fixed q-value of 0.21 nm^{-1} for dextran 40 concentrations ranging from 10 to 40%w/w. (*D*) $g_2(t)$ functions at the same q-value for 20%w/w of dextran, Ficoll, and sucrose. Solid lines represent fits based on Eq. **1**. Error bar determination is described in *Materials and Methods*. The ferritin schematic is adapted from PDB ID:2w0o (67).

X-ray pulse trains containing 200 and 310 pulses with a spacing of 440 and 220 ns interacted with the sample, and pulse-resolved scattering patterns were recorded with the Adaptive Gain Integrating Pixel Detector (AGIPD), positioned at 7.15 m and 7.68 m from the sample, respectively. This configuration provided access to wavevectors q in the range of 0.1 to 1 nm^{-1} as well as 0.075 to 1 nm^{-1} and enabled measurements on timescales from 0.44 to 88 μs and 0.22 to 69 μs.

To reduce radiation damage and beam-induced heating, the X-ray intensity was strongly attenuated, resulting in photon fluxes of 10^7 to 10^8 photons per pulse incident on the sample. The sample volume was refreshed for each pulse train, ensuring that the total X-ray dose and dose rate remained below established damage thresholds (42, 43). Statistically robust data were obtained by averaging scattering patterns and autocorrelation functions from more than 12,000 distinct positions across multiple capillaries. In addition to the MHz-XPCS experiments, complementary small-angle X-ray scattering (SAXS) measurements were performed at the DELTA synchrotron radiation facility at TU Dortmund (68).

The observed dynamics can be attributed exclusively to ferritin, as no correlation and thus no dynamics were detected in the two-time correlation functions of the pure crowder solutions (*SI Appendix*, Fig. S1). Protein dynamics were analyzed by calculating intensity autocorrelation functions, $g_2(q, t)$, from the temporal intensity fluctuations of the speckle patterns recorded within individual X-ray pulse trains. Fig. 1*B* presents an example of the resulting q-dependent $g_2(q, t)$ functions, where q refers to the momentum transfer as $q = 4\pi/\lambda \sin(\theta)$ with 2θ denoting the scattering angle and λ indicating the X-ray wavelength. All $g_2(q, t)$ functions were collected at room temperature. The solid lines represent fits using the Kohlrausch–Williams–Watts (KWW) function (69):

$$g_2(q, t) = 1 + \beta(q) \exp[-2\,(\Gamma(q)\,t)^{\alpha}], \qquad [1]$$

where $\beta(q)$ denotes the q-dependent speckle contrast, modeled following refs. 70 and 71, $\Gamma(q)$ is the q-dependent relaxation rate, and α is the KWW exponent. All correlation functions are well described with $\alpha = 0.9$ indicating slightly subdiffusive behavior, consistent with previous observations for the diffusion of nanoparticles, proteins, and fluorescent tracers in solutions containing soft polymers (72–74). Further details on extracting the $g_2(q, t)$ are provided in *Materials and Methods*.

Fig. 1*C* shows the $g_2(t)$ functions of ferritin in dextran 40 solutions at varying concentrations. Fig. 1*D* compares

Downloaded from https://www.pnas.org by Michelle Dargasz on July 30, 2026 from IP address 217.83.180.133.

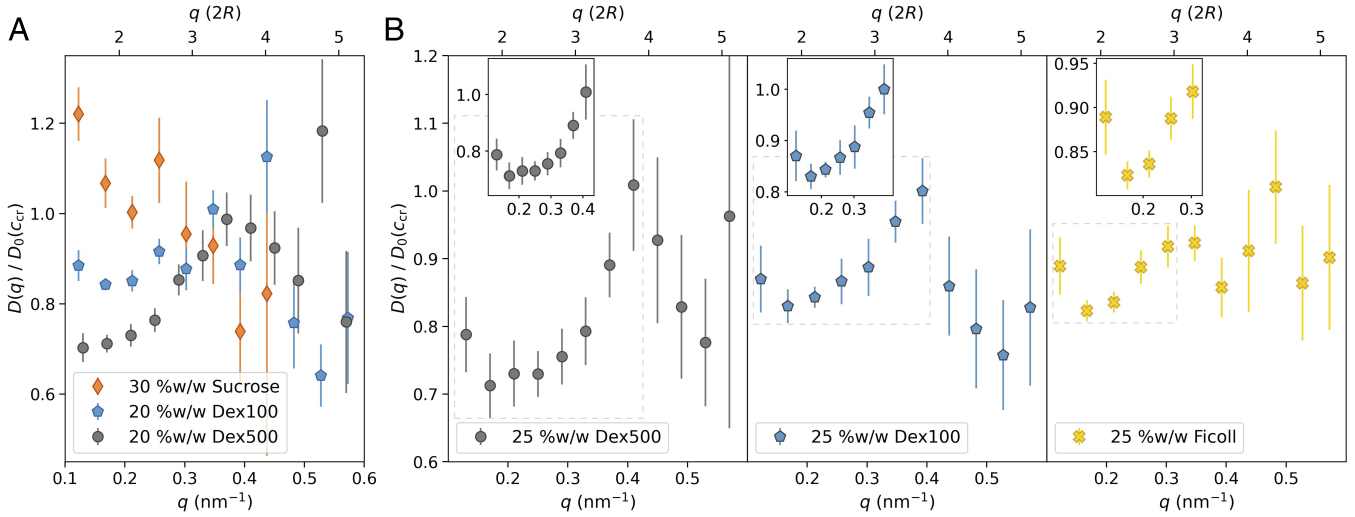


Fig. 2. Extracted q-dependent collective diffusion coefficients $D(q) = \Gamma(q)/q^2$ of ferritin in different crowder solutions, normalized to $D_0(c_{cr})$ for comparison. $D_0(c_{cr})$ was derived from Eq. **2**, with the respective values summarized in *SI Appendix*, Table S2. (*A*) $D(q)/D_0(c_{cr})$ for ferritin in solution with 30%w/w sucrose and 20%w/w dextran 100 and dextran 500. (*B*) $D(q)/D_0(c_{cr})$ in 25%w/w dextran 500 (*Left*), dextran 100 (*Middle*), and Ficoll (*Right*), with *Insets* zooming into the low-to-intermediate q-range showing the most pronounced changes. Error bars were obtained from least-squares fits of the g_2-functions.

ferritin dynamics in solutions containing different crowders at 20%w/w. In sucrose solutions, ferritin exhibits significantly faster dynamics than in polysaccharide-based solutions, primarily due to differences in solution viscosity (75, 76). Ficoll, with its highly branched architecture, elevates viscosity less than dextran, resulting in less pronounced ferritin slowing.

Depletion-Induced Attraction in Polysaccharide Solutions Hinders Collective Protein Motion on Mesoscales. In crowded solutions at high particle concentrations, protein dynamics are governed by both direct protein–protein interactions and indirect hydrodynamic interactions mediated by the solvent (77). These interactions give rise to a wavevector-dependent collective diffusion coefficient, $D(q)$, which can be related to the static structure factor $S(q)$, the hydrodynamic function $H(q)$, and the diffusion coefficient $D_0(c_{cr})$ of the protein in crowder solutions in the absence of protein–protein interactions (77)

$$D(q) = D_0(c_{cr}) \cdot \frac{H(q)}{S(q)}. \qquad [2]$$

In our experiment, reliable data are obtained across the range $q = 0.1$ to $0.57\ \mathrm{nm}^{-1}$, corresponding to length scales from approximately five to one ferritin diameters, respectively. Since XPCS probes density–density correlations shaped by interparticle interactions, the measured $D(q)$ directly reflects collective protein dynamics (see *SI Appendix* for details). The collective diffusion coefficient is extracted from exponential fits of the intensity autocorrelation functions, g_2, via $D(q) = \Gamma(q)/q^2$.

Fig. 2*A* compares the experimentally determined $D(q)$ of ferritin in solutions containing sucrose, dextran 100, and dextran 500. For ferritin in sucrose solution, $D(q)$ decreases with increasing q. Within the framework of Eq. **2**, such behavior is characteristic of systems dominated by repulsive protein–protein interactions (*SI Appendix*, Fig. S3) and is consistent with recent measurements of collective ferritin diffusion in aqueous solution (42). These findings are consistent with previous studies reporting that the addition of sucrose renders protein systems slightly more repulsive (78, 79).

In contrast, the $D(q)$ of ferritin in dextran 100 and dextran 500 increases from low to intermediate q, deviating markedly from the monotonic behavior expected for purely repulsive systems. Fig. 2*B* illustrates this effect for ferritin in solutions containing 25%w/w of dextran 500, dextran 100, and Ficoll. Comparing the low-q region ($q \approx 0.2\ \mathrm{nm}^{-1}$) with an intermediate q-range ($q \approx 0.3$ to $0.4\ \mathrm{nm}^{-1}$), a pronounced depression of $D(q)$ at low q is observed for dextran 500, a weaker but similar trend for dextran 100, and at most a marginal effect for Ficoll. A modest concentration dependence is also present, for example when comparing 10%w/w and 20%w/w (*SI Appendix*, Fig. S4), but this effect is substantially weaker than the molecular-weight dependence, likely reflecting the narrower concentration range explored.

With the relation given by Eq. **2**, an increase of $D(q)$ from low to intermediate wavevectors corresponds to a reduction of the inferred $S(q)$ at low q, consistent with the emergence of effective attractive interactions on mesoscopic length scales. The observed low-q suppression of $D(q)$ therefore indicates the presence of enhanced interprotein attraction in polysaccharide solutions.

In systems containing polymeric crowders, depletion interactions provide a well-established mechanism to induce short-range attraction. As polymers lose configurational entropy near protein surfaces, polymer-depleted regions form around the particles (23–25). When these regions overlap, the excluded volume for the polymers is reduced, increasing the system's entropy and generating an effective attractive force between proteins. Thus, in our system, the polymers present at elevated concentrations induce depletion interactions between the ferritin molecules.

Classical theories of semidilute polymer solutions predict depletion interactions to be largely independent of polymer molecular weight. In contrast, our experiments with dextran reveal a pronounced molecular-weight dependence. We attribute this discrepancy to the branched architecture of dextran, which likely modifies depletion behavior relative to that of linear polymers.

Thus, our experimental data show that depletion-induced attraction suppresses collective ferritin dynamics in polysaccharide solutions on mesoscopic length scales of approximately 2 to 3 ferritin diameters. The strength of this suppression depends

Downloaded from https://www.pnas.org by Michelle Dargasz on July 30, 2026 from IP address 217.83.180.133.

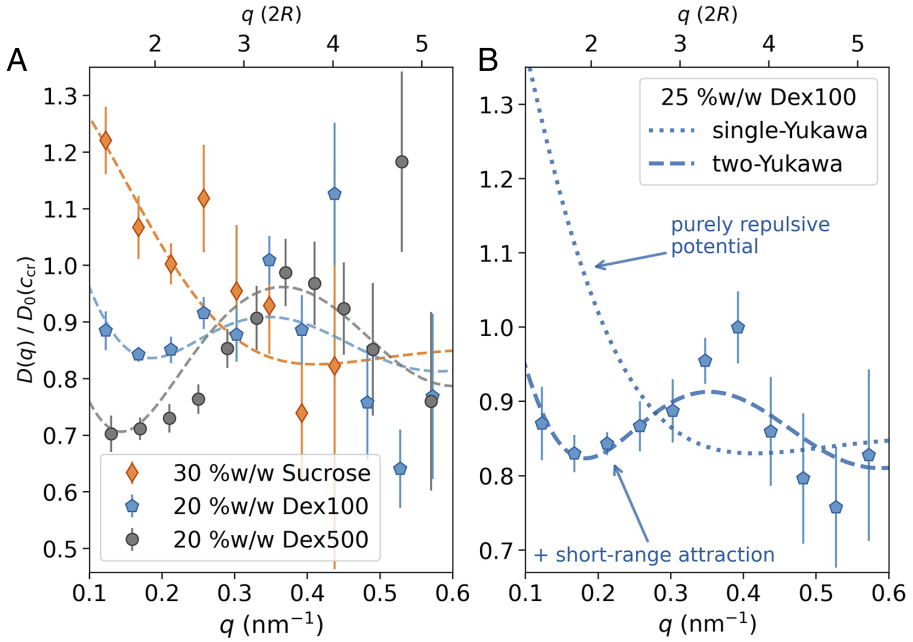


Fig. 3. Approximation of the experimental $D(q)/D_0(c_{cr})$ using simplified interparticle interaction potentials. (*A*) Experimental $D(q)/D_0(c_{cr})$ of ferritin in sucrose and dextran solutions compared with modeled $D(q)/D_0(c_{cr})$ (dashed lines). The modeled curves are calculated using a single-Yukawa potential for sucrose, capturing predominantly long-range repulsive interactions, and a two-Yukawa potential for dextran, which includes an additional short-range attractive contribution. (*B*) Comparison of modeled $D(q)/D_0(c_{cr})$ obtained using a purely repulsive single-Yukawa potential (dotted line) and a two-Yukawa potential with identical repulsive parameters plus an added short-range attraction (dashed line). Inclusion of an attractive interaction is required to reproduce the experimentally observed low-q behavior of $D(q)/D_0(c_{cr})$.

primarily on polysaccharide molecular weight and structure, while its concentration dependence is comparatively weak over the explored range.

Theoretical Approximation of Experimental $D(q)$ Based on Interparticle Interaction Potentials. To extract quantitative insight from the experimental $D(q)$, theoretical modeling of the data is performed. For this purpose we exploit the relation between $D(q)$, $S(q)$, and $H(q)$ given in Eq. **2**. Specifically, we compute the ratio $H(q)/S(q)$ using simplified theoretical models for the particle–particle interaction potential, as described in *SI Appendix*. We employ this approach as a reliable determination of the ferritin–ferritin structure factor from SAXS is not straightforward in the present ferritin-crowder mixtures, since the measured scattering contains ferritin-crowder cross-correlations that cannot be removed through background subtraction. While XPCS primarily probes the dominant intensity fluctuations arising from ferritin dynamics, the extraction of interaction-induced structural modulations in $S(q)$ relies on comparatively small deviations from unity and therefore remains sensitive to such cross-correlation contributions (see *SI Appendix* for details). The hydrodynamic function $H(q)$ is obtained using the $\delta\gamma$ expansion of Beenakker and Mazur (80, 81) (see *SI Appendix* for details). This approximation treats many-body hydrodynamic interactions in concentrated dispersions by relating $H(q)$ to the static structure factor $S(q)$ and the particle volume fraction, thereby accounting for the leading solvent-mediated hydrodynamic coupling beyond the dilute limit. It assumes spherical particles, equilibrium pair-averaged structural correlations, and a continuum-solvent description. We therefore use it as a coarse-grained approximation for the hydrodynamic contribution to $D(q)$, rather than as a microscopic description of crowder-specific flow fields.

To describe the predominantly repulsive interactions of ferritin in sucrose solution, a single-Yukawa potential is employed. In contrast, ferritin-polysaccharide mixtures require the inclusion of short-range attraction, which we model using a two-Yukawa potential. This coarse-grained form, commonly used for globular protein solutions, captures the competition between short-range attraction and long-range repulsion (82, 83). The use of a two-Yukawa potential is consistent with the experimentally observed low-q flattening or modest increase of $D(q \to 0)$, systematically found across the polysaccharide datasets.

The reduced form of the interaction potentials is given in *SI Appendix*, Eq. **S6**. Optimization of the potential parameters enables simultaneous determination of $S(q)$ and $H(q)$. To limit fitting freedom, the repulsive part is held fixed across datasets, while only the attractive term is varied with polymer concentration to reflect depletion effects. The resulting interaction potentials are shown in *SI Appendix*, Fig. S7, with fitted parameters summarized in *SI Appendix*, Table S2, and the corresponding modeled $D(q)$ displayed in *SI Appendix*, Fig. S5.

Despite the simplicity and empirical nature of this approach—and the fact that the true depletion potential is not expected to follow a two-Yukawa form exactly (84)—the calculated $D(q)$ agrees reasonably well with the experimental data (Fig. 3*A*). Fig. 3*B* further compares the modeled $D(q)$ obtained using a single- and a two-Yukawa potential with experimental data for ferritin in 25%w/w dextran 100. A purely repulsive single-Yukawa potential fails to reproduce the observed behavior, whereas inclusion of a short-range attractive term provides a reasonable approximation (*SI Appendix*, Fig. S6). We emphasize that this modeling is intended as an interpretive framework to classify experimentally observed trends, rather than as a unique or microscopic description of the underlying more complex interaction potentials.

Downloaded from https://www.pnas.org by Michelle Dargasz on July 30, 2026 from IP address 217.83.180.133.

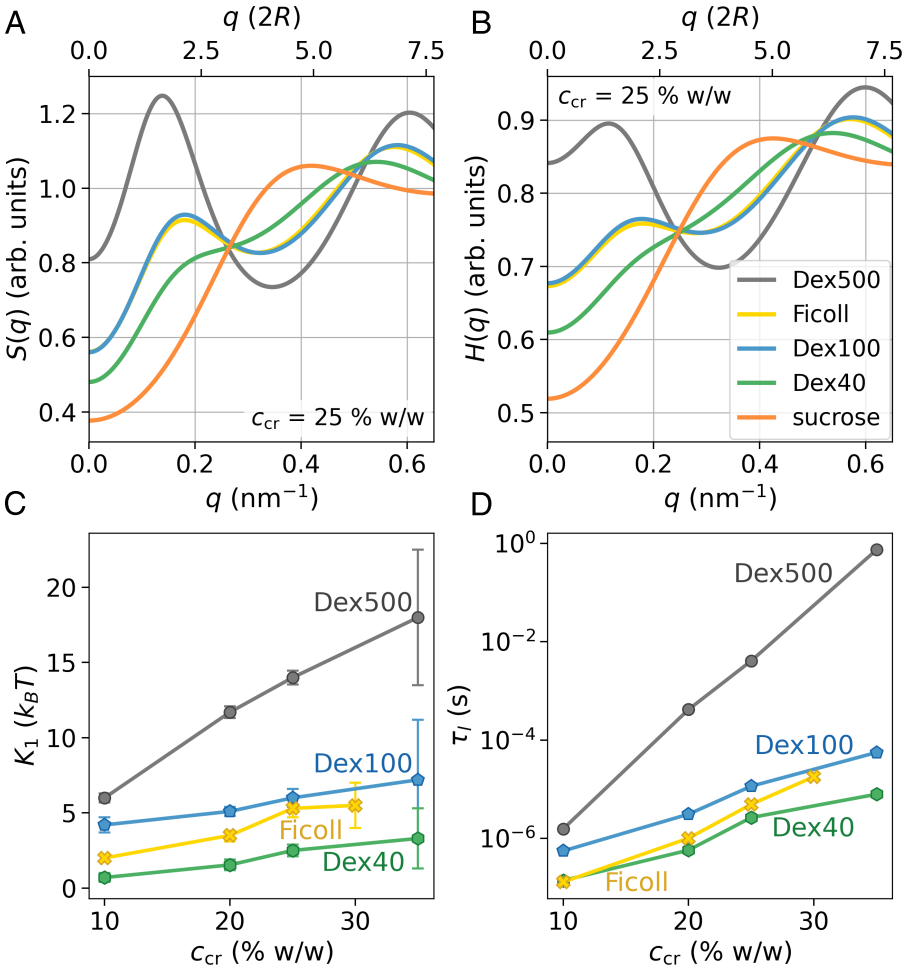


Fig. 4. Effects of crowder molecular weight and concentration on the attraction strength between ferritin molecules. (*A*) Modeled static structure factor $S(q)$ and (*B*) hydrodynamic function $H(q)$ using a two-Yukawa potential for ferritin in solutions containing different crowders at a concentration of c_{cr} = 25%w/w. (*C*) Attractive potential strength parameter K_1, extracted from modeling the experimental $D(q)$ via Eq. **2** as a function of crowder concentration. Error bars are estimated by varying K_1 within the experimental uncertainty of $D(q)$ while keeping all other potential parameters fixed. (*D*) Model-derived characteristic escape or residence time of transient ferritin associations stabilized by depletion-induced short-range attraction in polysaccharide solutions, calculated using Eq. **3**, as a function of c_{cr}.

***D*(*q*) Points to IRO Formation Arising from Competing Long-Range Repulsion and Depletion-Driven Short-Range Attraction.** Our model indicates that the coexistence of the depletion-induced short-range attraction and long-range repulsion leads to the emergence of intermediate-range order (IRO) of ferritin molecules. This organization is inferred from the characteristic low-q suppression of the collective diffusion coefficient $D(q)$ and its dependence on polymer molecular weight.

In protein solutions, repulsive interactions mainly arise from steric exclusion and electrostatics. At the ionic strength employed here, electrostatic interactions are largely screened and therefore short-ranged. In addition, polymer crowders can generate longer-range repulsive interactions. This so-called free-polymer-induced repulsion originates from a weak entropic preference of polymer chain ends for impenetrable interfaces. As two surfaces approach each other, perturbation of this end-enrichment leads to an imbalance in osmotic pressure, giving rise to a nonlocal, mesoscopic repulsive interaction (85–87).

IRO is characterized by spatial correlations extending over length scales of approximately two to three protein diameters. These correlations arise from the competition of interactions rather than from stable aggregation or clustering (35, 88). They correspond to transient, dynamically exchanging protein assemblies in which particles continuously associate and dissociate (35). Consequently, this organization remains highly dynamic, with structural fluctuations occurring on the microsecond timescale, consistent with the temporal window accessed by our XPCS experiments.

Such intermediate-range structural organization is expected to suppress collective protein mobility. Thus, the observed mesoscale suppression of $D(q)$ can be understood as a manifestation of de Gennes narrowing arising from depletion-induced intermediate-range structural organization (89). Related forms of IRO have been reported for concentrated lysozyme (90, 91) and monoclonal antibody (mAb) solutions (92), where enhanced attractive interactions arise either from high protein concentrations or from specific interprotein interactions.

The inferred intermediate-range organization is reflected in the estimated structure factors $S(q)$ (Fig. 4*A*) and hydrodynamic functions $H(q)$ (Fig. 4*B*) obtained from the empirical modeling of the experimental $D(q)$. In these quantities, intermediate-range organization appears as a low-q contribution, whereas the peak at $q \approx 0.4$ to 0.6 nm^{-1} corresponds to typical nearest-neighbor distances between ferritin molecules in solution, consistent with independent experimental observations (see *SI Appendix*, Figs. S2 and S3 and ref. 42).

Downloaded from https://www.pnas.org by Michelle Dargasz on July 30, 2026 from IP address 217.83.180.133.

Depletion Attraction Scales with Molecular Weight and Crowder Concentration. The inferred structure factors $S(q)$ and hydrodynamic functions $H(q)$, obtained from empirical modeling of the experimental $D(q)$ for ferritin in 25%w/w crowder solutions (Fig. 4 *A* and *B*), indicate that depletion-induced short-range attraction becomes increasingly pronounced with rising polysaccharide molecular weight. This behavior is reflected in the enhanced low-q contribution of both quantities and mirrors the molecular-weight dependence observed directly in the experimental collective diffusion coefficient $D(q)$ (Fig. 2). When examined as a function of crowder concentration, the inferred $S(q)$ and $H(q)$ exhibit qualitatively similar trends (*SI Appendix*, Fig. S9), but with substantially smaller amplitudes, consistent with the comparatively weak concentration dependence observed in the experimental dynamics.

Since $H(q) = 1$ corresponds to the absence of hydrodynamic interactions (77), deviations toward lower values quantify the degree of hydrodynamic hindrance arising from correlated particle motion. The increase of $H(q)$ at low q therefore reflects a reduction in hydrodynamic hindrance associated with transient mesoscale organization. This coupling between structural correlations and hydrodynamic interactions is well established and reflects the fact that correlated particle motion can give rise to more coherent flow patterns and reduced mutual interference, thereby modifying the effective hydrodynamic drag experienced by the proteins.

The hydrodynamic function also provides access to the sedimentation coefficient, since $H(q \to 0) = K = V_{\mathrm{sed}}/V_0$, where V_{sed} is the mean sedimentation velocity in a concentrated dispersion and V_0 the single-particle sedimentation velocity (40). Sedimentation is an essential mode of mass transport, playing a central role in the intracellular distribution of biomolecules (93, 94) and in regulating phase separation. Compared with sucrose solutions, where repulsive interactions dominate, polysaccharide solutions such as dextran 500 show enhanced sedimentation coefficients K (Fig. 4*B*). This increase indicates that short-range attraction introduced by macromolecular crowding can promote more efficient transport processes and potentially facilitate phase separation.

Fig. 4*C* shows the attractive potential strength K_1, extracted as a fit parameter from the two-Yukawa potential (*SI Appendix*, Eq. S6) for all solutions, illustrating that depletion-induced attraction strengthens with molecular weight and concentration. This trend is consistent with the deepening of the interaction potential minimum inferred from the modeling (*SI Appendix*, Fig. S7). An approximately linear increase of K_1 with concentration would be expected for depletion interactions induced by small crowders in the dilute regime. However, given the substantial uncertainties at highest concentrations, a deviation from linearity including a flattening that would be expected for depletion attraction in the semidilute to concentrated regime, remains equally compatible with the extracted parameters.

Following the approach of ref. 95, the potentials further allow an approximate estimation of the lifetimes of protein complexes stabilized by IRO, by considering the characteristic escape time of two particles from a potential well. For the rather shallow potentials to be considered here, we make use of an expression for the lifetime derived in ref. 96:

$$\tau_{\mathrm{I}} = \frac{\Delta^2}{D_{\mathrm{S}}(c_{\mathrm{cr}})}\,\frac{1}{U^2}\left(\exp\left(U\right) - 1\right) - \frac{1}{U}, \qquad [3]$$

where $\Delta \sim 0.1\sigma$, with $\sigma = 11.8$ nm corresponding to the ferritin diameter (97) and U denotes the minimum of the potential in units $k_{\mathrm{B}}T$. $D_{\mathrm{S}}(c_{\mathrm{cr}})$ is the self-diffusion coefficient of ferritin in crowder solutions for varying crowder concentrations. In principle, the self-diffusion coefficient corresponds to the limit $D(q \to \infty)$. However, due to limited data reliability at large q, we approximate the self-diffusion coefficient by evaluating our experimentally measured $D(q)$ at $q = 0.44\,\mathrm{nm}^{-1}$, which lies just below the position of the structure factor peak, where we infer $S(q) \approx 1$. The corresponding estimated lifetimes are shown in Fig. 4*D*. Increasing dextran molecular weights leads to stronger depletion-induced attraction and, consequently, longer-lived transient ferritin complexes. The estimated lifetimes based on the model-derived interaction potential are consistent with the relaxation times measured directly by MHz-XPCS. In particular, for dextran 500 at low q, the correlation functions do not fully decay within the accessible time window (*SI Appendix*, Fig. S10), indicating rather slow fluctuations associated with the IRO. We note, however, that the relaxation times are q-dependent collective quantities reflecting the decay of density fluctuations, related to the characteristic escape time τ_{I} only indirectly, as the transient associations suppress $D(q)$ in the relevant q-range and thereby increase the measured relaxation times.

This observation carries important implications for biological systems. Although macromolecular crowding is generally associated with reduced association rate constants due to slowed diffusion, this effect can be offset by enhanced intermolecular attraction—such as depletion-induced forces—which can accelerate binding (98–100). The pronounced increase in attractive interactions observed here under crowded conditions may therefore strongly influence protein–protein association dynamics, including processes such as enzymatic catalysis and cytokine-mediated immune signaling (101). Because both the strength of attraction and the lifetimes of associated complexes scale with crowder molecular weight and concentration, our findings may help reconcile the diverse and sometimes contradictory effects of crowding reported in the literature (102, 103).

Self-Diffusion Is Strongly Influenced by Micro- and Macroscopic Viscosity Variations Arising from Depletion Effects. To assess the impact of crowders on single-protein diffusion, the microscopic self-diffusion coefficient of ferritin approximated from experimental XPCS data, $D(q = 0.44\ \mathrm{nm}^{-1}, c_{\mathrm{cr}})$, was compared with the macroscopic diffusion coefficient $D_{\mathrm{SE}}(c_{\mathrm{cr}})$. The latter was calculated using the Stokes–Einstein equation, based on the experimentally determined bulk viscosities of the crowder solutions and the hydrodynamic radius of ferritin. The concentration dependence of $D_{\mathrm{SE}}(c_{\mathrm{cr}})$ is shown in Fig. 5*B* and exhibits a pronounced dependence on crowder molecular weight, reflecting the strong influence of polymer size on macroscopic viscosity. In contrast, the microscopic self-diffusion coefficient $D(q = 0.44\ \mathrm{nm}^{-1}, c_{\mathrm{cr}})$ exhibits no pronounced molecular weight dependence (Fig. 5*A*). This disparity indicates that, under crowded conditions, local polymer architecture and short-range interactions—rather than overall chain length that governs bulk viscosity—play a dominant role in regulating protein mobility on microscopic length scales.

To further probe the discrepancy between $D(q = 0.44\ \mathrm{nm}^{-1}, c_{\mathrm{cr}})$ and $D_{\mathrm{SE}}(c_{\mathrm{cr}})$, we analyzed their ratio as a function of the normalized crowder concentration c/c^* (Fig. 5*C*). This representation allows us to assign the observed effects to specific crowder concentration regimes, independent of crowder molecular weight and architecture. The results show that $D(q = 0.44\ \mathrm{nm}^{-1})/D_{\mathrm{SE}}$ does not scale with bulk viscosity and instead exhibits a nonmonotonic concentration dependence,

Downloaded from https://www.pnas.org by Michelle Dargasz on July 30, 2026 from IP address 217.83.180.133.

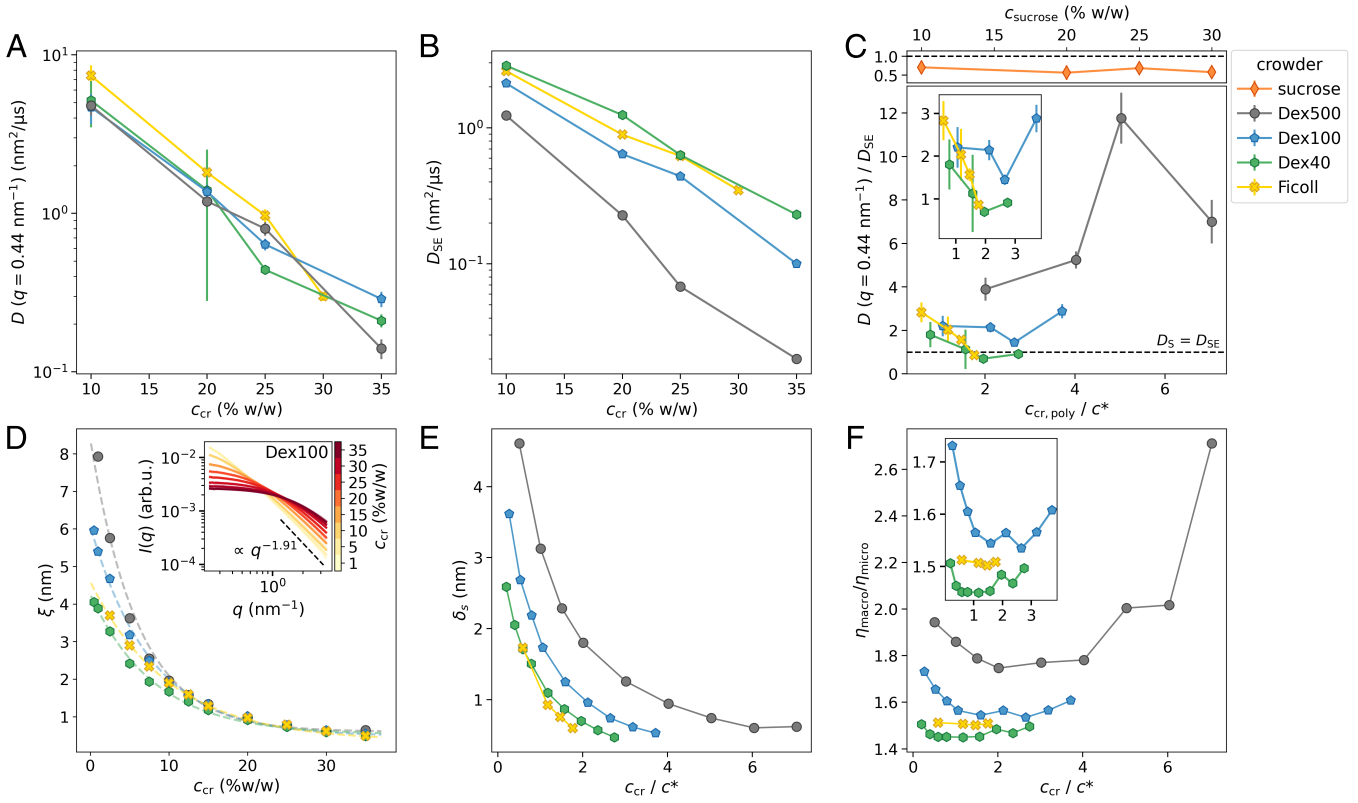


Fig. 5. Polysaccharide concentration and depletion effects on ferritin self-diffusion. (*A*) $D(q = 0.44\ \mathrm{nm}^{-1})$ as an approximation for the microscopic self-diffusion coefficient, and (*B*) macroscopic Stokes–Einstein self-diffusion coefficient D_{SE} as a function of crowder concentration c_{cr}. Error bars, obtained from error propagation of $D(q)$ fits and viscosity uncertainties, are smaller than symbols when not visible. (*C*) Ratio of microscopic to macroscopic self-diffusion coefficients as a function of polysaccharide concentration $c_{cr,poly}$ normalized by overlap concentration value c^*, whereas the ratio for sucrose is shown separately at the top as a function of sucrose concentration. The *Inset* highlights the two smaller dextrans and Ficoll. Error bars result from error propagation. (*D*) Correlation length $\xi(c_{cr})$ of crowder solutions obtained by fitting SAXS intensities of pure crowder solutions with Eq. **4**, dashed lines serve as visual guide. The *Inset* shows example SAXS data for dextran 100. (*E*) Depletion layer thickness δ_S calculated using *SI Appendix*, Eq. S11. (*F*) Ratio of macroscopic to microscopic viscosity as a function of normalized crowder concentration (c_{cr}/c^*). Microscopic viscosity values were calculated using *SI Appendix*, Eq. S12. The *Inset* again focuses on the two smaller dextrans and Ficoll.

with an initial decrease followed by an upturn for $c/c^* \geq 2$. According to Table 1, $c^{**} \approx 2.5$ to $3.5\,c^*$, indicating that this turning point coincides with the transition to the concentrated regime. The *Inset* highlights the ratio for Ficoll and dextran 40/100, showing only modest variations. The upturn appears reproducibly for all dextrans but not for Ficoll, possibly because the explored concentration range for Ficoll did not exceed $2c^*$, or because entanglements are absent in highly concentrated Ficoll solutions. At high crowder concentrations, $D(q = 0.44\ \mathrm{nm}^{-1})$ of dextran 500 exceeds the prediction of $D_{SE}(c_{cr})$ by up to a factor of eight, highlighting a pronounced decoupling between microscopic and macroscopic transport in high-M_W polymer-crowded environments.

The *Upper* panel of Fig. 5*C* displays the concentration-dependent ratio of microscopic to macroscopic self-diffusion for sucrose, evaluated using the experimental $D(q)$ at the largest reliable q-value at $\approx 0.35\ \mathrm{nm}^{-1}$. The macroscopic diffusion coefficient D_{SE} was calculated using literature values for the viscosity at the corresponding temperature (104). Within experimental uncertainties, this ratio remains nearly constant and slightly below unity over the entire concentration range. We attribute this systematic offset to the evaluation of D_{micro} at a q-value near the structure-factor peak in this purely repulsive system, where $D(q)$ is suppressed; extrapolation to the true $q \rightarrow \infty$ limit would likely shift the ratio closer to unity.

Although the decrease-to-increase crossover in the diffusion ratio is not sharply defined in every individual dataset, a consistent qualitative change is observed for polymeric crowders around $c \approx 2c^*$. This crossover behavior is absent for sucrose, highlighting the distinct role of polymer overlap and depletion effects in regulating protein self-diffusion on the microscopic scale.

To elucidate the origin of this behavior, we determined key parameters relevant to protein-polymer solutions. In the semidilute regime ($c > c^*$, see Table 1) the correlation length ξ replaces the polymer's radius of gyration as the characteristic structural length scale governing the depletion layer thickness (105). ξ defines the distance beyond which polymer–polymer interactions are screened by neighboring chains and was extracted by fitting measured SAXS curves of pure crowder solutions using an Ornstein-Zernike-like function (105–107):

$$I(q) = \frac{I(0)}{1 + (q\,\xi)^b}, \qquad [4]$$

where ξ and b are fitting parameters. The extracted correlation lengths are shown in Fig. 5*D*. The *Inset* provides the experimental SAXS curves alongside corresponding fits following Eq. **4** for dextran 100. Since the correlation length defines the depletion layer thickness δ_s in the semidilute regime, this parameter was calculated based on our determined ξ following the approaches

Downloaded from https://www.pnas.org by Michelle Dargasz on July 30, 2026 from IP address 217.83.180.133.

outlined in refs. 99 and 108–110. The corresponding equations are provided in *SI Appendix*. Theoretically estimated δ_s values as a function of normalized crowder concentration (c_{cr}/c^*) are shown in Fig. 5*E*. Following the approach of Tuinier et al. (111–114), the viscosity reduction within the depletion layer, caused by the locally reduced macromolecule concentration and hereafter referred to as the microscopic viscosity (η_{micro}), was determined from the measured macroscopic viscosity (η_{macro}), the solvent viscosity, and δ_s. Details of this calculation are provided in *SI Appendix*. The concentration dependence of both viscosity parameters is shown in *SI Appendix*, Fig. S11.

The resulting concentration-dependent ratio $\eta_{macro}/\eta_{micro}$ is shown in Fig. 5*F*, exhibiting a qualitatively similar tendency with a decrease at intermediate concentrations followed by an increase at concentrations around $c \gtrsim 2\,c^*$.

This analysis indicates that the nonmonotonic behavior reflects an interplay between microscopic and macroscopic viscosities mediated by depletion effects. Within the depletion layer surrounding the protein, from which macromolecules are excluded, the local microscopic viscosity (η_{micro}) is reduced relative to the bulk. At low crowder concentrations, the comparatively thick depletion layer facilitates faster self-diffusion of ferritin. With increasing crowder concentration, the polymer correlation length ξ decreases and the depletion layer progressively shrinks (Fig. 5 *D* and *E*). This increasingly constrains protein motion and results in a pronounced decrease of the microscopic protein diffusion coefficient $D(q = 0.44\ \mathrm{nm}^{-1})$, which becomes increasingly dominated by the rising macroscopic bulk viscosity.

Above ~2 to 3 c^*, the system enters the concentrated regime, where further increases in concentration primarily raise polymer density rather than extending the correlation range. Consequently, the depletion-layer thickness approaches an asymptotic limit (Fig. 5*E*), while the macroscopic viscosity continues to rise steeply. As a result, $D_{SE}(c_{cr})$ decreases more rapidly, producing the observed upturn in $D(q = 0.44\ \mathrm{nm}^{-1})/D_{SE}$. Dextran 500 reaches this regime at lower c/c^*, consistent with a stronger, entanglement-driven rise in macroscopic viscosity over the probed range. In contrast, sucrose shows no comparable crossover, consistent with the absence of depletion interactions on nanoscopic length scales.

It should be noted that most of the data lie in the regime $2R > \xi$, where microscopic diffusion is expected to remain close to the macroscopic Stokes–Einstein value. This likely explains why the absolute deviations observed in Fig. 5*C* remain relatively modest, while still being physically meaningful rather than trivial. At the same time, the absolute values shown in Fig. 5*F* differ by a factor of two or more from the experimental values in Fig. 5*C*, indicating that additional mechanisms beyond a simple depletion-layer picture must contribute to the observed behavior.

Enhanced nanoparticle diffusion in macromolecular crowder solutions is well documented and has been attributed to the fact that nanoparticles probe the local polymer structure rather than the bulk rheological properties of the solution (39). We therefore hypothesize that our experiments capture a combination of this established enhancement mechanism together with the influence of a nanoscopic depletion layer, resulting in the observed nonmonotonic concentration dependence. These effects are revealed by the high sensitivity of XPCS to molecular-scale dynamics, which enables us to resolve contributions from local structural features that are less accessible with conventional optical techniques.

Discussion

This study demonstrates that different types of crowder molecules induce distinct effects on protein dynamics. For ferritin, sucrose primarily preserves repulsive protein–protein interactions, whereas polysaccharide crowders introduce additional short-range attractions via depletion interactions, a well-established feature of protein-polymer mixtures. These attractions drive the emergence of IRO in ferritin-polysaccharide solutions, a universal effect observed for both dextran and Ficoll. Our results thus provide experimental validation of the simulation results by Riest et al. (40), which predicted that systems with short-range attraction combined with long-range repulsion exhibit unusual collective diffusion and hydrodynamic behavior, characterized by a low-q IRO in $S(q)$.

Despite their distinct conformations in solution—Ficoll forming compact, highly branched coils and dextran adopting more flexible, extended structures (20, 52)—short-range attraction consistently emerged. Increasing the molecular weight of dextran enhances these attractive interactions, giving rise to more stable and longer-lived ferritin complexes. This observation underscores that even variations in molecular weight within a single class of crowders can substantially modify crowding-induced effects on protein dynamics.

Self-diffusion measurements on both macroscopic and microscopic scales revealed pronounced differences, with the ratio of microscopic to macroscopic diffusion coefficients displaying a nonmonotonic dependence on crowder concentration. This behavior arises from the interplay between local depletion effects and bulk viscosity: At low concentrations, the shrinking depletion layer reduces self-diffusion, whereas beyond the semidilute regime, the steep increase in macroscopic viscosity becomes dominant. Normalization by the overlap concentration c^* produced a universal scaling behavior, with a turning point around $2c^*$, beyond which macroscopic viscosity overrides depletion-induced mobility enhancements.

Our investigation of ferritin under crowded conditions demonstrates that nanoscale protein dynamics are strongly shaped by: i) the interplay between proteins and crowders, including depletion interactions, ii) crowder type (e.g., small spheres vs. polymers) and its concentration as well as concentration-dependent structure, and iii) the crowder molecular weight. As a result, even commonly used crowding agents can induce nontrivial and system-specific behaviors, emphasizing the multifaceted nature of crowding. These insights provide a framework for reconciling the diverse and sometimes contradictory reports on protein behavior under crowded conditions, including enzymatic activity and protein association (16–19, 115–120).

Ultimately, this work highlights the necessity of integrating polymer physics and depletion theory alongside excluded volume effects into models of crowded environments, as these factors not only govern structural organization but also influence protein dynamics.

Materials and Methods

Sample Preparation. Ferritin was purchased from Sigma Aldrich and corresponds to ferritin from equine spleen in saline solution (CAS: 9007-73-2) with an initial protein concentration of $c = 71$ mg/ml. To increase the protein concentration, 8 ml of this solution was centrifuged at 5,000 g and 1.5 ml at 10,000 g for 15 min using 30 kDa Millipore filters. Using SAXS calibration curves of ferritin solutions of known concentration, the resulting ferritin concentration was determined to be 110 mg/ml and 265 mg/ml.

Downloaded from https://www.pnas.org by Michelle Dargasz on July 30, 2026 from IP address 217.83.180.133.

Stock solutions of dextran 40, dextran 100, and dextran 500 (Roth, CAS: 9004-54-0) were prepared in concentrations of 20, 40, 43.75, and 50%w/w as well as of Ficoll®400 (Sigma Aldrich, CAS: 26873-85-8) and sucrose (Sigma Aldrich, CAS: 57-50-1) in concentrations of 20, 40, 50, and 60%w/w by dissolving them in 103 mM saline solution with a pH value of 7.

To obtain a final dextran concentration of 35%w/w in the sample, the 265 mg/ml ferritin solution was mixed with the 43.75%w/w dextran stock in a 20%: 80% volume ratio. All the other stock solutions were mixed 50%: 50% with the 110 mg/ml ferritin solution. The resulting crowder concentrations in the sample are therefore 10, 20, 25, and 35%w/w using dextran as a crowder and 10, 20, 25, and 30%w/w using sucrose and Ficoll as crowders. The ferritin concentration remains constant at approx. 55 mg/ml. The solutions were filled into quartz capillaries with an outer diameter of 1.5 mm and a wall thickness of 10 μm.

Experimental Setup. Two experiments were carried out at the Materials Imaging and Dynamics (MID) instrument of European XFEL to collect the data presented. In both cases the small-angle X-ray scattering (SAXS) configuration was used. The first experiment was performed using the pink beam with a photon energy of 9 keV. 200 pulses per train were delivered with a repetition rate of 2.25 MHz, which corresponds to a pulse spacing of 440 ns. For the second experiment the pink beam with a photon energy of 10 keV and a higher repetition rate of 4.5 MHz (220 ns pulse spacing) was available. The intertrain repetition rate was 10 Hz in both experiments. Using compound refractive lenses (CRL), the beam was focused to 14.5 μm and 14.2 μm in diameter, respectively. The values for the beamsize were obtained by fitting the speckle contrast in conjunction with an effective X-ray bandwidth of $\Delta E/E = 13 \times 10^{-3}$ and 9×10^{-3}, respectively. Using a scanning speed of 0.4 mm/s of the Fast Solid Sample Scanner (FSSS) ensures the refreshment of the sample volume in between the trains, as described in ref. 41. The data acquisition was realized by the AGIPD (121, 122), which was positioned 7.15 m and 7.68 m behind the sample. Thus, a q-range of 0.1 to 1 nm^{-1} and 0.075 to 1 nm^{-1} was accessible, respectively. All measurements were performed at room temperature (23 °C).

XPCS Calculations. The scattering of coherent X-rays by the ferritin particles within the sample system generates a speckle pattern that varies over time as a result of particle motion. To analyze the dynamics of ferritin, the fluctuating intensities measured experimentally at two distinct times, t_1 and t_2, were correlated. This approach employs two-time correlation functions of the form (123–125):

$$C(q, t_1, t_2) = \frac{\langle I(q, t_1) I(q, t_2) \rangle_{\text{pix}}}{\langle I(q, t_1) \rangle_{\text{pix}} \langle I(q, t_2) \rangle_{\text{pix}}}, \quad [5]$$

where $\langle \ldots \rangle_{\text{pix}}$ indicate the average of all detector pixels within the same q-range. In the first experiment, the q-binning was set to $\Delta q = 0.045$ nm^{-1}, in the second to $\Delta q = 0.04$ nm^{-1}. The calculations were performed utilizing the EXtra-speckle data processing pipeline (126) coupled to DAMNIT tool (127) developed at EuXFEL. For a sufficient signal-to-noise ratio, data were collected and averaged over several thousand trains. The intensity autocorrelation functions, $g_2(q, t) = \langle C(q, t_1, t_1 + t) \rangle_{t_1}$, were extracted by performing horizontal cuts along the t_1 axis, starting from the diagonal (128). Based on the SD of the fluctuating contrast values of the TTC, a weighted average over trains and times was calculated to determine the final $g_2(q, t)$ function. The error bars correspond to the square root of the inverse of the summed weights.

Data, Materials, and Software Availability. Data recorded at the European XFEL are available at DOIs: 10.22003/XFEL.EU-DATA-003348-00 (129) and 10.22003/XFEL.EU-DATA-005397-00 (130). Data collected at DELTA are available at DOI: 10.5281/zenodo.21222886 (131).

ACKNOWLEDGMENTS. We acknowledge European X-ray free electron laser (XFEL) in Schenefeld, Germany, for providing X-ray free-electron laser beamtime at Materials Imaging and Dynamics instrument and would like to thank the staff for their support. The data presented here were collected during two beamtimes allocated to proposals 3348 and 5397. This work was supported by the Maxwell computational resources of the Deutsches Elektronen-Synchrotron DESY, Hamburg, Germany. Furthermore, we acknowledge the machine group of Dortunder Elektronenspeicherringanlage (DELTA) for providing machine group for providing synchrotron radiation and for technical support. We thank Marvin Kowalski, Jenny Schrage, Pia Kwiasowski, Maximilian Senft, Prince Prabhu Rajaiah, Lara Reichart, and Chang Hee Woo for their collaboration during beamtime and Randeer Gautam for the discussion of the experimental results. We acknowledge the Bundesministerium für Forschung, Technik und Raumfahrt (05K19PS1, 05K20PSA, and 05K22PS1) (to C.G.); 05K19VTB (to F.Z. and F.S.), and the DFG-ANR funding programme of the Deutsche Forschungsgemeinschaft and the Agence Nationale de la Recherche (SCHR700/28-1, SCHR700/42-1, ANR-16-CE92-0009, and SCHR700/48-1) (to F.Z. and F.S.). We acknowledge financial support by the consortium DAPHNE4NFDI in association with the German National Research Data Infrastructure NFDI (project No. 460248799, DFG 40/1). A.G., I.A., and F.P. acknowledge funding from the European Union's Horizon Europe research and innovation programme under the Marie Skłodowska-Curie grant agreement Nos. 101081419 (PhD Research and Innovation in Synchrotron Methods and Applications in Sweden) (I.A. and F.P.) and 101149230 (Uncovering hidden structures in protein crystallization with coherent X-rays) (A.G. and F.P.). F.P. acknowledges financial support by the Swedish National Research Council (Vetenskapsrådet) under Grant Nos. 2019-05542 and 2023-05339 and within the Röntgen-Ångström Cluster Grant No. 2019-06075, and the kind financial support from Knut och Alice Wallenberg foundation (Grant. No. 2023.0052). This research is supported by the Center of Molecular Water Science of DESY in an Early Science Project, the MaxWater initiative of the Max-Planck-Gesellschaft (Project No. CTS21:1589), and Carl Tryggers and the Wenner-Gren Foundations (Project No. UPD2021-0144).

Author affiliations: [a]Department Physik, Universität Siegen, Siegen 57072, Germany; [b]Deutsches Elektronen-Synchrotron, Hamburg 22603, Germany; [c]Institut für Angewandte Physik, Universität Tübingen, Tübingen 72076, Germany; [d]Department of Physics, AlbaNova University Center, Stockholm University, Stockholm 10691, Sweden; [e]European X-Ray Free-Electron Laser Facility, Schenefeld 22869, Germany; and [f]Fakultät Physik/Dortmunder Elektronenspeicherringanlage, Technische Universität Dortmund, Dortmund 44221, Germany

Author contributions: M.D., F.P., F.S., M.P., and C.G. designed research; M.D., N.D.A., S.R., A.G., S.T., J.M., W.J., A.L., M.R.A, M.B., J.S., I.A., F.U., F.B., J.H., U.B., J.-E.P., A.R.-F., J.W., R.S., M.Y., A.Z., A.M., F.L., F.Z., M.P., and C.G. performed research; J.M., A.L., F.B., and J.W. provided the data analysis pipeline; M.D. analyzed data; S.R., F.L., F.P., F.Z., F.S., M.P., and C.G. discussed data; J.M., W.J., F.B., J.H., U.B., J.-E.P., A.R.-F., R.S., M.Y., A.Z., and A.M. operated materials imaging and dynamics at European X-ray free electron laser facility instrument; M.D., N.D.A., A.G., M.B., and J.S. prepared the samples; and M.D., M.P., and C.G. wrote the paper and all authors provided input for the paper.

1. R. J. Ellis, Macromolecular crowding: Obvious but underappreciated. *Trends Biochem. Sci.* **26**, 597–604 (2001).
2. T. C. Laurent, A. Ogston, The interaction between polysaccharides and other macromolecules. 4. The osmotic pressure of mixtures of serum albumin and hyaluronic acid. *Biochem. J.* **89**, 249 (1963).
3. A. P. Minton, Excluded volume as a determinant of macromolecular structure and reactivity. *Biopolymers* **20**, 2093–2120 (1981).
4. A. P. Minton, Influence of excluded volume upon macromolecular structure and associations in "crowded" media. *Curr. Opin. Biotechnol.* **8**, 65–69 (1997).
5. C. Alfano *et al.*, Molecular crowding: The history and development of a scientific paradigm. *Chem. Rev.* **124**, 3186–3219 (2024).
6. M. Bonucci, T. Shu, L. J. Holt, How it feels in a cell. *Trends Cell Biol.* **33**, 924–938 (2023).
7. G. Grassmann *et al.*, Computational approaches to predict protein-protein interactions in crowded cellular environments. *Chem. Rev.* **124**, 3932–3977 (2024).
8. A. Mathur, R. Ghosh, A. Nunes-Alves, Recent progress in modeling and simulation of biomolecular crowding and condensation inside cells. *J. Chem. Inf. Model.* **64**, 9063–9081 (2024).
9. M. Grimaldo, F. Roosen-Runge, F. Zhang, F. Schreiber, T. Seydel, Dynamics of proteins in solution. *Q. Rev. Biophys.* **52**, e7 (2019).
10. I. Yu *et al.*, Biomolecular interactions modulate macromolecular structure and dynamics in atomistic model of a bacterial cytoplasm. *eLife* **5**, e19274 (2016).
11. F. Roosen-Runge *et al.*, Protein self-diffusion in crowded solutions. *Proc. Natl. Acad. Sci. U.S.A.* **108**, 11815–11820 (2011).
12. K. Luby-Phelps, Cytoarchitecture and physical properties of cytoplasm: Volume, viscosity, diffusion, intracellular surface area. *Int. Rev. Cytol.* **192**, 189–221 (1999).

Downloaded from https://www.pnas.org by Michelle Dargasz on July 30, 2026 from IP address 217.83.180.133.

13. M. Heinen *et al*., Viscosity and diffusion: Crowding and salt effects in protein solutions. *Soft Matter* **8**, 1404–1419 (2012).
14. J. A. Dix, A. Verkman, Crowding effects on diffusion in solutions and cells. *Annu. Rev. Biophys.* **37**, 247–263 (2008).
15. D. Gnutt, S. Ebbinghaus, The macromolecular crowding effect - from in vitro into the cell. *Biol. Chem.* **397**, 37–44 (2016).
16. L. Homchaudhuri, N. Sarma, R. Swaminathan, Effect of crowding by dextrans and Ficolls on the rate of alkaline phosphatase-catalyzed hydrolysis: A size-dependent investigation. *Biopolymers* **83**, 477–486 (2006).
17. B. K. Derham, J. J. Harding, The effect of the presence of globular proteins and elongated polymers on enzyme activity. *Biochim. Biophys. Acta Proteins Proteomics* **1764**, 1000–1006 (2006).
18. G. Ren, Z. Lin, C.-I. Tsou, C.-c. Wang, Effects of macromolecular crowding on the unfolding and the refolding of d-glyceraldehyde-3-phosophospate dehydrogenase. *J. Protein Chem.* **22**, 431–439 (2003).
19. J. R. Wenner, V. A. Bloomfield, Crowding effects on EcoRV kinetics and binding. *Biophys. J.* **77**, 3234–3241 (1999).
20. V. T. Ranganathan, S. Bazmi, S. Wallin, Y. Liu, A. Yethiraj, Is Ficoll a colloid or polymer? A multitechnique study of a prototypical excluded-volume macromolecular crowder. *Macromolecules* **55**, 9103–9112 (2022).
21. S. Biswas, J. Kundu, S. K. Mukherjee, P. K. Chowdhury, Mixed macromolecular crowding: A protein and solvent perspective. *ACS Omega* **3**, 4316–4330 (2018).
22. F. I. Rusinga, D. D. Weis, Soft interactions and volume exclusion by polymeric crowders can stabilize or destabilize transient structure in disordered proteins depending on polymer concentration. *Proteins Struct. Funct. Bioinf.* **85**, 1468–1479 (2017).
23. S. Asakura, F. Oosawa, On interaction between two bodies immersed in a solution of macromolecules. *J. Chem. Phys.* **22**, 1255–1256 (1954).
24. A. Vrij, Polymers at interfaces and the interactions in colloidal dispersions. *Pure Appl. Chem.* **48**, 471–483 (1976).
25. H. N. Lekkerkerker, R. Tuinier, M. Vis, *Colloids and the Depletion Interaction* (Springer Nature, ed. 2, 2024).
26. R. Roth, Fundamental measure theory for hard-sphere mixtures: A review. *J. Phys. Condens. Matter* **22**, 063102 (2010).
27. R. Roth, R. Evans, S. Dietrich, Depletion potential in hard-sphere mixtures: Theory and applications. *Phys. Rev. E* **62**, 5360 (2000).
28. C. Bechinger, D. Rudhardt, P. Leiderer, R. Roth, S. Dietrich, Understanding depletion forces beyond entropy. *Phys. Rev. Lett.* **83**, 3960 (1999).
29. M. Fuchs, K. S. Schweizer, Structure of colloid-polymer suspensions. *J. Phys. Condens. Matter* **14**, R239 (2002).
30. B. Neu, H. J. Meiselman, Depletion interactions in polymer solutions promote red blood cell adhesion to albumin-coated surfaces. *Biochim. Biophys. Acta Gen. Subj.* **1760**, 1772–1779 (2006).
31. N. J. Smith, P. A. Williams, Depletion flocculation of polystyrene latices by water-soluble polymers. *J. Chem. Soc. Faraday Trans.* **91**, 1483–1489 (1995).
32. H. Zhang, D. Kong, W. Zhang, H. Liu, Depletion attraction in colloidal and bacterial systems. *Front. Mater.* **10**, 1206819 (2023).
33. C. Gögelein, G. Nägele, J. Buitenhuis, R. Tuinier, J. K. Dhont, Polymer depletion-driven cluster aggregation and initial phase separation in charged nanosized colloids. *J. Chem. Phys.* **130**, 204905 (2009).
34. R. Tuinier, J. Dhont, C. De Kruif, Depletion-induced phase separation of aggregated whey protein colloids by an exocellular polysaccharide. *Langmuir* **16**, 1497–1507 (2000).
35. Y. Liu *et al*., Lysozyme protein solution with an intermediate range order structure. *J. Phys. Chem. B* **115**, 7238–7247 (2011a).
36. P. D. Godfrin, N. E. Valadez-Pérez, R. Castaneda-Priego, N. J. Wagner, Y. Liu, Generalized phase behavior of cluster formation in colloidal dispersions with competing interactions. *Soft Matter* **10**, 5061–5071 (2014).
37. S. von Bülow, M. Siggel, M. Linke, G. Hummer, Dynamic cluster formation determines viscosity and diffusion in dense protein solutions. *Proc. Natl. Acad. Sci. U.S.A.* **116**, 9843–9852 (2019).
38. L. H. Cai, S. Panyukov, M. Rubinstein, Mobility of nonsticky nanoparticles in polymer liquids. *Macromolecules* **44**, 7853–7863 (2011).
39. I. Kohli, A. Mukhopadhyay, Diffusion of nanoparticles in semidilute polymer solutions: Effect of different length scales. *Macromolecules* **45**, 6143–6149 (2012).
40. J. Riest, G. Nägele, Short-time dynamics in dispersions with competing short-range attraction and long-range repulsion. *Soft Matter* **11**, 9273–9280 (2015).
41. M. Reiser *et al*., Resolving molecular diffusion and aggregation of antibody proteins with megahertz X-ray free-electron laser pulses. *Nat. Commun.* **13**, 5528 (2022).
42. A. Girelli *et al*., Coherent X-rays reveal anomalous molecular diffusion and cage effects in crowded protein solutions. *Nat. Commun.* **16**, 10814 (2025).
43. Lipoprotein diffusion in dense yolk plasma is governed by softness, hydrodynamics, and caging: Insights from MHz-XPCS. *Proc. Natl. Acad. Sci. U.S.A.* **123**, e2519681123 (2026).
44. E. C. Theil, *The Ferritin Family of Iron Storage Proteins* (John Wiley & Sons, Ltd., 1990), pp. 421–449.
45. P. M. Harrison, P. Arosio, The ferritins: Molecular properties, iron storage function and cellular regulation. *Biochim. Biophys. Acta Bioenerg.* **1275**, 161–203 (1996).
46. N. D. Chasteen, P. M. Harrison, The ferritins: Molecular properties, iron storage function and cellular regulation. *J. Struct. Biol.* **126**, 182–194 (1999).
47. A. Mohanty, M. K, S. S. Jena, R. K. Behera, Kinetics of ferritin self-assembly by laser light scattering: Impact of subunit concentration, pH, and ionic strength. *Biomacromolecules* **22**, 1389–1398 (2021).
48. M. Q. Rodrigues, P. M. Alves, A. Roldão, Functionalizing ferritin nanoparticles for vaccine development. *Pharmaceutics* **13**, 1621 (2021).
49. M. Khoshnejad, H. Parhiz, V. V. Shuvaev, I. J. Dmochowski, V. R. Muzykantov, Ferritin-based drug delivery systems: Hybrid nanocarriers for vascular immunotargeting. *J. Control. Release* **282**, 13–24 (2018).
50. R. Lucignano *et al*., Human ferritin nanocarriers for drug-delivery: A molecular view of the disassembly process. *Int. J. Biol. Macromol.* **277**, 134373 (2024).
51. X. Liu, S. Oh, M. W. Kirschner, The uniformity and stability of cellular mass density in mammalian cell culture. *Front. Cell Dev. Biol.* **10**, 1017499 (2022).
52. I. Kohli, A. Mukhopadhyay, Contrasting nanoparticle diffusion in branched polymer and particulate solutions: More than just volume fraction. *Soft Matter* **9**, 8974–8979 (2013).
53. C. Olsson, J. Swenson, Structural comparison between sucrose and trehalose in aqueous solution. *J. Phys. Chem. B* **124**, 3074–3082 (2020).
54. V. T. Ranganathan *et al*., Is Ficoll a colloid or polymer? A multitechnique study of a prototypical excluded-volume macromolecular crowder.. *Macromolecules* **55**, 9103–9112 (2022).
55. K. A. Granath, Solution properties of branched dextrans. *J. Colloid Sci.* **13**, 308–328 (1958).
56. A. B. Fulton, How crowded is the cytoplasm? *Cell* **30**, 345–347 (1982).
57. V. R. Gade *et al*., Polysomes and mRNA control the biophysical properties of the eukaryotic cytoplasm. *Cell Rep.* **44**, 116204 (2025).
58. S. J. Spencer, V. T. Ranganathan, A. Yethiraj, G. T. Andrews, Concentration dependence of elastic and viscoelastic properties of aqueous solutions of Ficoll and bovine serum albumin by brillouin light scattering spectroscopy. *Langmuir* **40**, 4615–4622 (2024).
59. A. Madsen *et al*., Materials Imaging and Dynamics (MID) instrument at the European X-ray Free-Electron Laser Facility. *J. Synchrotron Radiat.* **28**, 637–649 (2021).
60. N. D. Anthuparambil *et al*., Salt induced slowdown of kinetics and dynamics during thermal gelation of egg-yolk. *J. Chem. Phys.* **161**, 055102 (2024).
61. N. D. Anthuparambil *et al*., Exploring non-equilibrium processes and spatio-temporal scaling laws in heated egg yolk using coherent X-rays. *Nat. Commun.* **14**, 5580 (2023).
62. S. Timmermann *et al*., X-ray driven and intrinsic dynamics in protein gels. *Sci. Rep.* **13**, 11048 (2023).
63. Y. Chushkin *et al*., Probing cage relaxation in concentrated protein solutions by X-ray photon correlation spectroscopy. *Phys. Rev. Lett.* **129**, 238001 (2022).
64. A. Girelli *et al*., Microscopic dynamics of liquid-liquid phase separation and domain coarsening in a protein solution revealed by X-ray photon correlation spectroscopy. *Phys. Rev. Lett.* **126**, 138004 (2021).
65. N. Begam *et al*., Kinetics of network formation and heterogeneous dynamics of an egg white gel revealed by coherent X-ray scattering. *Phys. Rev. Lett.* **126**, 098001 (2021).
66. F. Dallari *et al*., Microsecond hydrodynamic interactions in dense colloidal dispersions probed at the European XFEL. *IUCrJ* **8**, 775–783 (2021).
67. N. de Val, J. P. Declercq, C. K. Limc, R. R. Crichton, Structural analysis of haemin demetallation by L-chain apoferritins. *J. Inorg. Biochem.* **112**, 77–84 (2012).
68. M. Dargasz *et al*., X-ray scattering at beamline BL2 of DELTA: Studies of lysozyme-lysozyme interaction in heavy water and structure formation in 1-hexanol. *J. Phys. Conf. Ser.* **2380**, 012031 (2022).
69. G. Williams, D. C. N. Watts, Non-symmetrical dielectric relaxation behaviour arising from a simple empirical decay function. *Trans. Faraday Soc.* **66**, 80–85 (1970).
70. S. Hruszkewycz *et al*., High contrast X-ray speckle from atomic-scale order in liquids and glasses. *Phys. Rev. Lett.* **109**, 185502 (2012).
71. F. Lehmkühler *et al*., Emergence of anomalous dynamics in soft matter probed at the European XFEL. *Proc. Natl. Acad. Sci. U.S.A.* **117**, 24110–24116 (2020).
72. R. A. Omari, A. M. Aneese, C. A. Grabowski, A. Mukhopadhyay, Diffusion of nanoparticles in semidilute and entangled polymer solutions. *J. Phys. Chem. B* **113**, 8449–8452 (2009).
73. D. S. Banks, C. Fradin, Anomalous diffusion of proteins due to molecular crowding. *Biophys. J.* **89**, 2960–2971 (2005).
74. H. Sanabria, Y. Kubota, M. N. Waxham, Multiple diffusion mechanisms due to nanostructuring in crowded environments. *Biophys. J.* **92**, 313–322 (2007).
75. J. Mazurkiewicz, M. Nowotny-Różańska, Viscosity of aqueous solutions of saccharides. *Pol. J. Food Nutr. Sci.* **48**, 171–180 (1998).
76. M. A. Masuelli, Dextrans in aqueous solution. Experimental review on intrinsic viscosity measurements and temperature effect. *J. Polym. Biopolym. Phys. Chem.* **1**, 13–21 (2013).
77. G. Nägele, On the dynamics and structure of charge-stabilized suspensions. *Phys. Rep.* **272**, 215–372 (1996).
78. K. Julius *et al*., Impact of macromolecular crowding and compression on protein-protein interactions and liquid-liquid phase separation phenomena. *Macromolecules* **52**, 1772–1784 (2019).
79. G. Yuan *et al*., Flow activation energy of high-concentration monoclonal antibody solutions and protein-protein interactions influenced by NaCl and sucrose. *Mol. Pharm.* **21**, 4553–4564 (2024).
80. C. Beenakker, P. Mazur, Diffusion of spheres in a concentrated suspension II. *Phys. A Stat. Mech. Appl.* **126**, 349–370 (1984).
81. C. Beenakker, P. Mazur, Self-diffusion of spheres in a concentrated suspension. *Phys. A Stat. Mech. Appl.* **120**, 388–410 (1983).
82. M. Broccio, D. Costa, Y. Liu, S. H. Chen, The structural properties of a two-Yukawa fluid: Simulation and analytical results. *J. Chem. Phys.* **124**, 084501 (2006).
83. S. H. Chen, M. Broccio, Y. Liu, E. Fratini, P. Baglioni, The two-Yukawa model and its applications: The cases of charged proteins and copolymer micellar solutions. *J. Appl. Crystallogr.* **40**, 321–326 (2007).
84. S. Ramakrishnan, M. Fuchs, K. S. Schweizer, C. F. Zukoski, Entropy driven phase transitions in colloid-polymer suspensions: Tests of depletion theories. *J. Chem. Phys.* **116**, 2201–2212 (2002).
85. A. Semenov, Theory of colloid stabilization in semidilute polymer solutions. *Macromolecules* **41**, 2243–2249 (2008).
86. A. Shvets, A. Semenov, Effective interactions between solid particles mediated by free polymer in solution. *J. Chem. Phys.* **139**, 054905 (2013).
87. A. Semenov, A. Shvets, Theory of colloid depletion stabilization by unattached and adsorbed polymers. *Soft Matter* **11**, 8863–8878 (2015).
88. F. Zhang *et al*., Effective interactions in protein solutions with and without clustering. *Phys. A Stat. Mech. Appl.* **650**, 129995 (2024).
89. P. G. De Gennes, Liquid dynamics and inelastic scattering of neutrons. *Physica* **25**, 825–839 (1959).
90. L. Porcar *et al*., Formation of the dynamic clusters in concentrated lysozyme protein solutions. *J. Phys. Chem. Lett.* **1**, 126–129 (2010).
91. Y. Liu *et al*., Lysozyme protein solution with an intermediate range order structure. *J. Phys. Chem. B* **115**, 7238–7247 (2011b).

Downloaded from https://www.pnas.org by Michelle Dargasz on July 30, 2026 from IP address 217.83.180.133.

92. E. J. Yearley *et al.*, Observation of small cluster formation in concentrated monoclonal antibody solutions and its implications to solution viscosity. *Biophys. J.* **106**, 1763–1770 (2014).
93. J. Li, H. J. Busscher, W. Norde, J. Sjollema, Analysis of the contribution of sedimentation to bacterial mass transport in a parallel plate flow chamber. *Colloids Surf. B Biointerfaces* **84**, 76–81 (2011).
94. P. M. Hinderliter *et al.*, ISDD: A computational model of particle sedimentation, diffusion and target cell dosimetry for in vitro toxicity studies. *Part. Fibre Toxicol.* **7**, 1–20 (2010).
95. F. Cardinaux *et al.*, Cluster-driven dynamical arrest in concentrated lysozyme solutions. *J. Phys. Chem. B* **115**, 7227–7237 (2011).
96. M. Abkenar, T. H. Gray, A. Zaccone, Dissociation rates from single-molecule pulling experiments under large thermal fluctuations or large applied force. *Phys. Rev. E.* **95**, 042413 (2017).
97. D. C. F. Wieland *et al.*, ASAXS measurements on ferritin and apoferritin at the bioSAXS beamline p12 (PETRA III, DESY). *J. Appl. Cryst.* **54**, 830–838 (2021).
98. A. M. Berezhkovskii, A. Szabo, Theory of crowding effects on bimolecular reaction rates. *J. Phys. Chem. B* **120**, 5998–6002 (2016).
99. F. Zosel, A. Soranno, K. J. Buholzer, D. Nettels, B. Schuler, Depletion interactions modulate the binding between disordered proteins in crowded environments. *Proc. Natl. Acad. Sci. U.S.A.* **117**, 13480–13489 (2020).
100. H. X. Zhou, G. Rivas, A. P. Minton, Macromolecular crowding and confinement: Biochemical, biophysical, and potential physiological consequences. *Annu. Rev. Biophys.* **37**, 375–397 (2008).
101. G. Schreiber, G. Haran, H. X. Zhou, Fundamental aspects of protein-protein association kinetics. *Chem. Rev.* **109**, 839–860 (2009).
102. I. M. Kuznetsova, K. K. Turoverov, V. N. Uversky, What macromolecular crowding can do to a protein. *Int. J. Mol. Sci.* **15**, 23090–23140 (2014).
103. S. Mittal, R. K. Chowhan, L. R. Singh, Macromolecular crowding: Macromolecules friend or foe. *Biochim. Biophys. Acta Gen. Subj.* **1850**, 1822–1831 (2015).
104. J. F. Swindells, C. Snyder, R. C. Hardy, P. Golden, *Viscosities of Sucrose Solutions at Various Temperatures: Tables of Recalculated Values* (US Department of commerce, National Bureau of standards, 1958), vol. 440.
105. R. Colby, Structure and linear viscoelasticity of flexible polymer solutions: Comparison of polyelectrolyte and neutral polymer solutions. *Rheol. Acta* **49**, 425–442 (2010).
106. J. S. Pedersen, P. Schurtenberger, Scattering functions of semidilute solutions of polymers in a good solvent. *J. Polym. Sci. B Polym. Phys.* **42**, 3081–3094 (2004).
107. J. S. Higgins, H. C. Benoit, *Polymers and Neutron Scattering* (Oxford University Press, 1994).
108. G. J. Fleer, A. M. Skvortsov, R. Tuinier, Mean-field equation for the depletion thickness. *Macromolecules* **36**, 7857–7872 (2003).
109. R. Tuinier, H. Lekkerkerker, D. Aarts, Interaction potential between two spheres mediated by excluded volume polymers. *Phys. Rev. E* **65**, 060801 (2002).
110. A. Hanke, E. Eisenriegler, S. Dietrich, Polymer depletion effects near mesoscopic particles. *Phys. Rev. E* **59**, 6853 (1999).
111. R. Tuinier, T. Taniguchi, Polymer depletion-induced slip near an interface. *J. Phys. Condens. Matter* **17**, L9–L14 (2005).
112. T. H. Fan, J. K. Dhont, R. Tuinier, Motion of a sphere through a polymer solution. *Phys. Rev. E* **75**, 011803 (2007).
113. T. H. Fan, B. Xie, R. Tuinier, Asymptotic analysis of tracer diffusivity in nonadsorbing polymer solutions. *Phys. Rev. E* **76**, 051405 (2007).
114. R. Tuinier, J. Dhont, T. H. Fan, How depletion affects sphere motion through solutions containing macromolecules. *Europhys. Lett.* **75**, 929 (2006).
115. M. Jiang, Z. Guo, Effects of macromolecular crowding on the intrinsic catalytic efficiency and structure of enterobactin-specific isochorismate synthase. *J. Am. Chem. Soc.* **129**, 730–731 (2007).
116. A. Dhar *et al.*, Structure, function, and folding of phosphoglycerate kinase are strongly perturbed by macromolecular crowding. *Proc. Natl. Acad. Sci. U.S.A.* **107**, 17586–17591 (2010).
117. M. G. Norris, N. Malys, What is the true enzyme kinetics in the biological system? An investigation of macromolecular crowding effect upon enzyme kinetics of glucose-6-phosphate dehydrogenase. *Biochem. Biophys. Res. Commun.* **405**, 388–392 (2011).
118. D. N. Okamoto *et al.*, Increase of SARS-CoV 3CL peptidase activity due to macro-molecular crowding effects in the milieu composition. *Biol. Chem.* **391**, 1461–1468 (2010).
119. I. Pastor *et al.*, Effect of crowding by dextrans on the hydrolysis of N-Succinyl-l-phenyl-Ala-p-nitroanilide catalyzed by α-chymotrypsin. *J. Phys. Chem. B* **115**, 1115–1121 (2011).
120. B. Van Den Berg, R. J. Ellis, C. M. Dobson, Effects of macromolecular crowding on protein folding and aggregation. *EMBO J.* **18**, 6927–6933 (1999).
121. A. Allahgholi *et al.*, The adaptive gain integrating pixel detector at the European XFEL. *J. Synchrotron Radiat.* **26**, 74–82 (2019).
122. J. Sztuk-Dambietz *et al.*, Operational experience with Adaptive Gain Integrating Pixel Detectors at European XFEL. *Front. Phys.* **11**, e1329378 (2024).
123. F. Lehmkühler, W. Roseker, G. Grübel, From femtoseconds to hours - Measuring dynamics over 18 orders of magnitude with coherent X-rays. *Appl. Sci.* **11**, 6179 (2021).
124. F. Perakis, C. Gutt, Towards molecular movies with X-ray photon correlation spectroscopy. *Phys. Chem. Chem. Phys.* **22**, 19443–19453 (2020).
125. M. Sutton, K. Laaziri, F. Livet, F. Bley, Using coherence to measure two-time correlation functions. *Opt. Express* **11**, 2268–2277 (2003).
126. A. Leonau *et al.*, A pipeline for megahertz X-ray photon correlation spectroscopy on soft matter samples at the MID instrument of European XFEL. *J. Synchrotron Rad.* **33**, 725–738 (2026).
127. Data Analysis group at the European XFEL, Damnit user documentation (2025). https://damnit.readthedocs.io/en/latest/. Accessed 2 September 2025.
128. O. Bikondoa, On the use of two-time correlation functions for X-ray photon correlation spectroscopy data analysis. *J. Appl. Crystallogr.* **50**, 357–368 (2017).
129. C. Gutt *et al.*, LTP - MHz XPCS enabled studies of dynamics, interactions and aggregation phenomena in protein solutions (derived from 3348) [Dataset]. European X-ray Free Electron Laser facility. https://doi.org/10.22003/XFEL.EU-DATA-003348-00. Deposited 13 Februrary 2023.
130. C. Gutt *et al.*, LTP - MHz XPCS enabled studies of dynamics, interactions and aggregation phenomena in protein solutions (derived from 5397) [Dataset]. European X-ray Free Electron Laser facility. https://doi.org/10.22003/XFEL.EU-DATA-005397-00. Deposited 27 November 2023.
131. M. Paulus *et al.*, Structural characterization of crowder solutions by SAXS [Dataset]. Zenodo. https://doi.org/10.5281/zenodo.21222886. Deposited 6 July 2026.

Downloaded from https://www.pnas.org by Michelle Dargasz on July 30, 2026 from IP address 217.83.180.133.